nature energy

ARTICLES

https://doi.org/10.1038/s41560-019-0492-1

Efficient hybrid colloidal quantum dot/organic solar cells mediated by near-infrared sensitizing small molecules

Se-Woong Baek[1,2,8], Sunhong Jun[3,8], Byeongsu Kim[4,8], Andrew H. Proppe[1,5,8], Olivier Ouellette[1], Oleksandr Voznyy[1], Changjo Kim[4], Junho Kim[2], Grant Walters[1], Jung Hoon Song[6], Sohee Jeong[6], Hye Ryung Byun[6], Mun Seok Jeong[6], Sjoerd Hoogland[1], F. Pelayo García de Arquer[1], Shana O. Kelley[5,7], Jung-Yong Lee[2,4*] and Edward H. Sargent[1*]

Solution-processed semiconductors are promising materials to realize optoelectronic devices that combine high performance with inexpensive manufacturing. In particular, the exploitation of colloidal quantum dots (CQDs) capable of harvesting infrared photons, in conjunction with visible-absorbing organic chromophores, has been demonstrated as an interesting route. Unfortunately, CQD/organic hybrid photovoltaics have been limited to power conversion efficiencies (PCEs) below 10% due to chemical mismatch and difficulties in facilitating charge collection. Here we devise a hybrid architecture that overcomes these limitations by introducing small molecules into the CQD/organic stacked structure. The small molecule complements CQD absorption and creates an exciton cascade with the host polymer, thus enabling efficient energy transfer and also promoting exciton dissociation at heterointerfaces. The resulting hybrid solar cells exhibit PCEs of 13.1% and retain over 80% of their initial PCE after 150 h of continuous operation unencapsulated, outperforming present air-processed solution-cast CQD/organic photovoltaics.

Solution-processed semiconductors such as perovskites[1], organics[2] and colloidal quantum dots (CQDs)[3] are materials that, with their distinctive photophysical and optoelectronic properties, enable the realization of next-generation photodetectors, light-emitting diodes and solar cells exhibiting programmable characteristics[4].

CQDs can be tuned in absorption across the solar spectrum via size-dependent quantum confinement. Advances in the last decade in CQD chemistry, surface passivation, film assembly and device architecture have led to the demonstration of CQD solar cells with certified power conversion efficiencies (PCEs) of 12% (ref. [5]). Most efficient CQD solar cells use a depleted heterojunction architecture consisting of a halide solution-exchanged CQD photoactive layer and a hole transport layer consisting of a thiol-exchanged CQD film[6].

In organic semiconductors, bulk-heterojunction (BHJ) architectures are often employed. Donor and acceptor molecules are intermixed at the nanoscale to generate heterojunctions throughout the active layer. This is required to overcome short exciton diffusion lengths within disordered polymers and small-molecule-based materials[2]. These diffusion lengths are usually limited to tens of nanometres—well below the absorption length of light in these materials.

Since hybrid CQD/organic solar cells were proposed[7], various strategies for CQD/organic heterostructures have been studied with the goal of combining the advantages of the two classes of materials and thereby achieving higher PCE and stability[8]. Many of these hybrid structures have demonstrated complementary absorption spectra, but studies have failed to exploit this to improve performance in optoelectronic devices due to poor charge transfer (CT) and carrier extraction efficiencies, limiting PCEs to below 10% (ref. [8]).

We revisited the CQD/polymer architecture with the goal of overcoming these challenges. Here, we sought to modify the polymer layer by mixing in a low-bandgap non-fullerene small molecule. The introduction of a small-molecule bridge into the polymer layer allowed us to increase the efficiency of exciton dissociation and funneling—as revealed using ultrafast transient absorption (TA) and photoluminescence excitation (PLE) spectroscopies, as well as external and internal quantum efficiency (IQE) measurements—and thereby enabled improved charge-extraction efficiencies exceeding 90% across the visible and near infrared. Due to absorption that is complementary in the host polymer versus the CQD film, photocurrents in hybrid devices are also improved.

Using this architecture, we achieve a PCE of 13.1%. In addition, we demonstrate devices having continuously stable operation (80% of initial PCE, t_{80}) of 150 h at their maximum power point (MPP), relying neither on an ultraviolet (UV) filter nor on encapsulation, outperforming prior air- and solution-processed CQD/organic photovoltaics.

Small molecule bridges

We began by considering architectures that could accommodate a CQD/polymer hybrid material configuration. CQD/polymer BHJ structures have been widely investigated to this end[8] and

[1]Department of Electrical and Computer Engineering, University of Toronto, Toronto, Ontario, Canada. [2]EEWS, KAIST, Daejeon, Republic of Korea. [3]Department of Chemistry, Northwestern University, Evanston, IL, USA. [4]School of Electrical Engineering, KAIST, Daejeon, Republic of Korea. [5]Department of Chemistry, University of Toronto, Toronto, Ontario, Canada. [6]Department of Energy Science, Sungkyunkwan University, Suwon, Republic of Korea. [7]Department of Pharmaceutical Sciences, Leslie Dan Faculty of Pharmacy, University of Toronto, Toronto, Ontario, Canada. [8]These authors contributed equally: Se-Woong Baek, Sunhong Jun, Byeongsu Kim, Andrew H. Proppe. *e-mail: jungyong.lee@kaist.ac.kr; ted.sargent@utoronto.ca

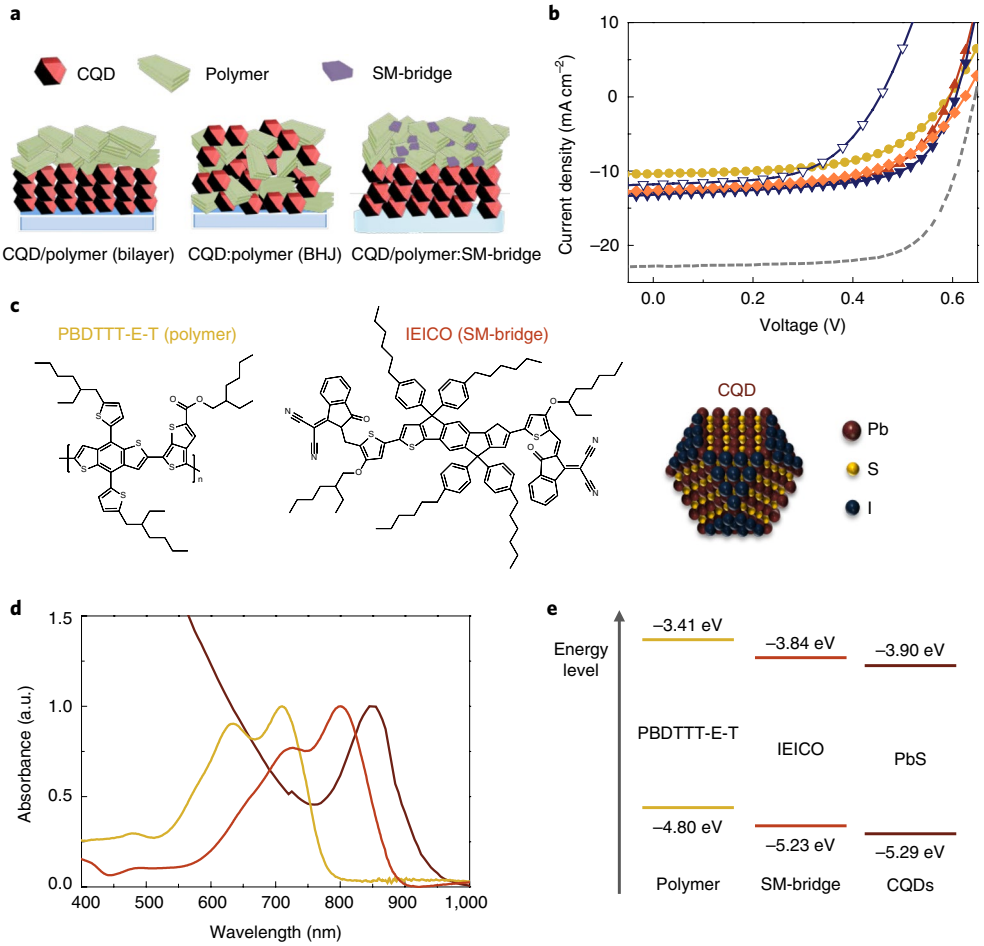

Fig. 1 | Hybrid CQD/polymer structure design strategy. a, Illustration of prior CQD/polymer (bilayer and BHJ) and proposed CQD/polymer–SM-bridge structures. **b**, *J*–*V* curves of CQD/EDT-treated CQD control device (grey dashed line), CQD/PTB7 (yellow), CQD/PTB7-Th (red), CQD/PDTD-DFBT (orange) and CQD/PBDTTT-E-T (blue filled triangles) and CQD–PBDTTT-E-T (BHJ) (blue open triangles) under AM 1.5 illumination. **c**, Illustration and molecular structure of the PBDTTT-E-T polymer, the IEICO SM-bridge and the iodide-passivated PbS CQDs. **d**, Absorbance spectra of CQD (brown), polymer (yellow) and SM-bridge (red) films. a.u., arbitrary units. **e**, Band alignment of polymer, SM-bridge and CQD films.

have exploited PDPPTPD[9], PDTPBT[10], P3HT[11,12], PDTPQx[13] and si-PCPDTBT[14] paired with various CQDs. In a bilayer configuration, on the other hand, a polymer layer is stacked vertically on a CQD film. With the goal of constructing an efficient CQD/polymer hybrid, we screened a range of p-type polymers and explored their combinations with CQDs both in BHJ and bilayer configurations. (Fig. 1a) We sought low-bandgap polymers[15–17] with absorption bands between approximately 550 and 850 nm that could complement those of the PbS CQDs and improve light harvesting (Supplementary Fig. 1).

Representative current density–voltage (*J*–*V*) curves and photovoltaic parameters of various CQD/polymer hybrids are shown in Fig. 1b and Supplementary Table 1, respectively. In these devices, active layers consisted of CQDs passivated with 1-ethyl-3-methylimidazolium iodide (EMII) ligands. PCEs of approximately 10% were obtained for CQD control devices using a top (hole-transporting) layer of CQDs treated with 1,2-ethanedithiol (EDT), a commonly used CQD bilayer architecture. When polymers are used instead of an EDT-CQD layer, all CQD/polymer bilayer combinations exhibited significantly lower performance, with PCEs below 5%. The short-circuit current (J_{sc}) reached only half of that of the CQD reference devices despite a similar total absorption. The external quantum efficiency (EQE) of the hybrid devices is particularly low in the wavelength range corresponding to absorption in the polymer, suggesting that photogenerated excitons fail to dissociate at polymer/CQD boundaries, and so carriers are not extracted efficiently[18] (Supplementary Fig. 1c). We also explored a suite of BHJ structures with the goal of overcoming limitations in exciton diffusion, dissociation and charge extraction (Fig. 1b). However, hybrid BHJ devices exhibited a lower performance than the bilayer structures, which we attributed to a poor CQD/polymer interpenetration network arising from the large surface energy difference between inorganic CQDs and polymers (Supplementary Fig. 2)[19], interfacial defect recombination at the CQD surface[20] and rapid geminate recombination at the halide CQD–polymer interface[21].

These findings led us to posit that introducing an auxiliary n-type organic semiconductor into the polymer could potentially reduce geminate recombination and assist charge transport to the CQD–polymer boundary by dissociating strongly bound excitons into free charge carriers. Hybrid p-type CQD/polymer structures employing [6,6]-phenyl-C_{61}-butyric acid methyl ester (PCBM) have been studied previously[22,23]; however, this approach failed to achieve high PCEs and resulted in poor stability due to the narrow absorption band of PCBM, the large driving energy for exciton separation at the CQD–PCBM interface (which severely limited the open-circuit voltage (V_{oc}))[24,25] and oxidation or dimerization of PCBM.

Ideally, well-designed molecular additives would exhibit an acceptor-like behaviour that would induce faster exciton dissociation

at interfaces and establish an energy gradient that could facilitate cascading energy transfer of excitons and electrons toward the n-type CQD film, acting as a bridge between the two materials. Recently, non-fullerene small molecules suitable for this application—exhibiting a low bandgap, distinctive absorption bands in the near infrared and compatibility with p-type polymers—have been reported[2]. We selected the small-molecule acceptor bridge (the SM-bridge) (2,2'-((2Z,2'Z)-((5,5'-bis(4,4,9,9-tetrakis)-4,9-dihydro-s-indaceno[1,2-b:5,6-b']dithiophene-2,7-diyl)bis(4-(2-ethylhexyl) oxy)thiophene-diyl)bis (methanylylene))bis-(3-oxo-2,3-dihydro-1H-indene-2,1-diylidenene)dimalononitrile (IEICO))[26] (Fig. 1c). With its 1.34 eV bandgap, the SM-bridge absorbs light between 600 and 900 nm and thus complements the absorption of the CQD/polymer hybrids (Fig. 1d). For the host p-type polymer, we selected PBDTTT-E-T, a copolymer of benzo[1,2-b:4,5-b']dithiophene (BDT) and thieno[3,4-b]thiophene (TT), because of the previously reported high-quality morphology of mixed solids of PBDTTT-E-T and IEICO[2].

To evaluate the energy levels of each material and verify that the proposed SM-bridge has a favourable band alignment with the polymer and CQD components, we performed ultraviolet photoelectron spectroscopy on its individual constituents (Supplementary Fig. 3). Halide-treated CQD films exhibit an n-type behaviour and a deeper conduction band (−3.90 eV) than that of the SM-bridge. The SM-bridge exhibits a highest occupied molecular orbital level of −5.23 eV and a lowest unoccupied molecular orbital level of −3.84 eV, straddled by the valence band of the CQDs and the lowest unoccupied molecular orbital level of the polymer (Fig. 1e). In this energy landscape, electrons photoexcited at the polymer and SM-bridge sites are transported towards the CQD layer.

Charge-carrier dynamics

We next sought to understand charge and energy transfer dynamics among the various organic and CQD components using a suite of spectroscopic techniques. (Fig. 2a, b) In photoluminescence (PL) emission experiments, photoexciting the polymer–SM-bridge mixed layer leads to increased emission from the SM-bridge (~870 nm), accompanied by reduced emission from the polymer donor (~760 nm), consistent with energy transfer from the polymer donor to the SM-bridge[27,28]. The spectral overlap of the SM-bridge emission and CQD absorption suggests energy transfer from the SM-bridge to the CQDs should also be favourable[28]. Normalized PL spectra show a shift in emission toward the CQD bandgap, indicative of energy transfer (Supplementary Fig. 4 and Supplementary Note 1)[29]. This indicates that the SM-bridge helps to form an energy funnel that facilitates transfer of excitons photogenerated in the polymer domains to the CQD layer.

To evaluate more clearly if energy transfer occurs from the organic to CQD domains, we carried out PLE spectroscopy on bilayer films consisting of polymer/CQDs and SM-bridge/CQDs, photoexciting the top surface of the stack (Fig. 2b). We prepared the CQD layer using larger-sized dots (excitonic peak ~1,050 nm) and monitored the PL emission at 1,200 nm, thus avoiding PL from the organics themselves. By photoexciting at wavelengths across the absorption range (500–950 nm), we recovered the shape of the static absorption spectrum of each organic molecule, revealing energy transfer from the molecules to the underlying CQD layer (Fig. 2c). Notably, in the normalized PLE spectra, we found that when we compared the ratio of the peak amplitude for emission originating from exciting the organic molecule (between 600 and 800 nm), compared to direct excitation of the CQDs (near 500 nm), this ratio is greater for the SM-bridge than for the polymer, indicating that energy transfer to the CQDs from the SM-bridge is more efficient compared to the polymer (Supplementary Fig. 4).

The type-II band alignment between the organic and the CQD layers indicates that excitons and electrons migrate from the organics to CQDs, and that hole transfer must occur from CQDs to organics (Fig. 1e). We probed this process using ultrafast transient absorption spectroscopy (TAS). TA spectra for hybrid/CQD films are shown in Fig. 2d. The generation of an excited-state population in the CQDs (evidenced by the CQD band-edge exciton bleach at 900 nm) is followed by the build-up of bleach signal at ~730 nm from the polymer (Supplementary Fig. 11), which appears at early delay times and becomes larger in amplitude over hundreds of picoseconds (Fig. 2d). This is consistent with hole transfer from photoexcited CQDs into the polymer layer (Supplementary Fig. 10 and Supplementary Table 2). Global fitting of the TA data with three decay associated spectra (DAS) and associated time constants gives an approximate hole transfer time of 270 ps (Fig. 2g). Similar TAS experiments on SM-bridge/CQD films show the absence of hole transfer from CQDs to the SM-bridge (Supplementary Figs. 5, 8 and 9), and bleaching of only the polymer component is observed in the same experiment for polymer–SM-bridge/CQD films, indicating the hole-transporting role of polymer domains (Supplementary Note 2).

In addition to exciton funneling, another important role of the SM-bridge is to serve as an electron acceptor at the polymer–SM-bridge interfaces. In the absence of the SM-bridge, energy transfer will be the dominant carrier migration mechanism in the polymer film. Due to the short exciton diffusion length within the disordered polymer film[30], the majority of excitons will be quenched before reaching the polymer–CQD interface (Supplementary Fig. 1). Acceptor-like molecules can help overcome this limitation by facilitating charge separation of the exciton at donor–acceptor interfaces through interfacial CT states, generating longer-lived free electrons and holes.

To investigate whether the incorporation of the SM-bridge into the polymer domains leads to such dynamics, we performed additional TAS experiments on the organic blends (photoexciting at 730 nm) (Fig. 2e,f) and again performed global analysis to extract DAS spectra[31], shown in Fig. 2h,i. We observe photo-induced absorption (PIA) signals for the blend that are longer-lived and redshifted compared to the unblended individual polymer and SM-bridge components, an observation that is characteristic of CT states in organic blends (Supplementary Figs. 11 and 12 and Supplementary Notes 3 and 4). We also found that this PIA signal is larger in amplitude when the organic blend is formed on top of the CQD layer, attributable to additional CT state formation at the organic–CQD interface (Fig. 2f and Supplementary Fig. 13)[32]. A similar PIA amplitude increase is also observed for the individual SM-bridge and polymer components when they are interfaced with the CQDs (Supplementary Fig. 12). The formation of these interfaces should favour exciton dissociation, enabling improved charge extraction under solar cell operation (Supplementary Figs. 11 and 14). We propose that the SM-bridge, in addition to serving as an exciton relay, serves as an electron acceptor from the polymer, diminishing exciton quenching within the polymer domains (Supplementary Notes 4 and 5).

Absorption and charge-extraction enhancement

We then sought to take advantage of the auspicious photo-induced carrier dynamics in the CQD/SM-bridge–polymer hybrids to build improved photovoltaic devices (Fig. 3a). CQD solids and polymer layers were sequentially deposited, forming the CQD/polymer heterostructure. SM-bridges were mixed into the polymer before its deposition. Atomic force microscopy (AFM) revealed rod-shaped grains of several tens of nanometres in polymer–SM-bridge interfaces (Supplementary Fig. 15)[33]. Cross-sectional transmission electron microscopy (TEM) shows the structure and thickness of each layer in the complete device: ZnO (30 nm)/CQDs (150 nm)/polymer (with or without SM-bridge, 65 nm)/MoO_3 (10 nm)/Ag (150 nm) (Fig. 3a). The elemental depth profiling measured via time

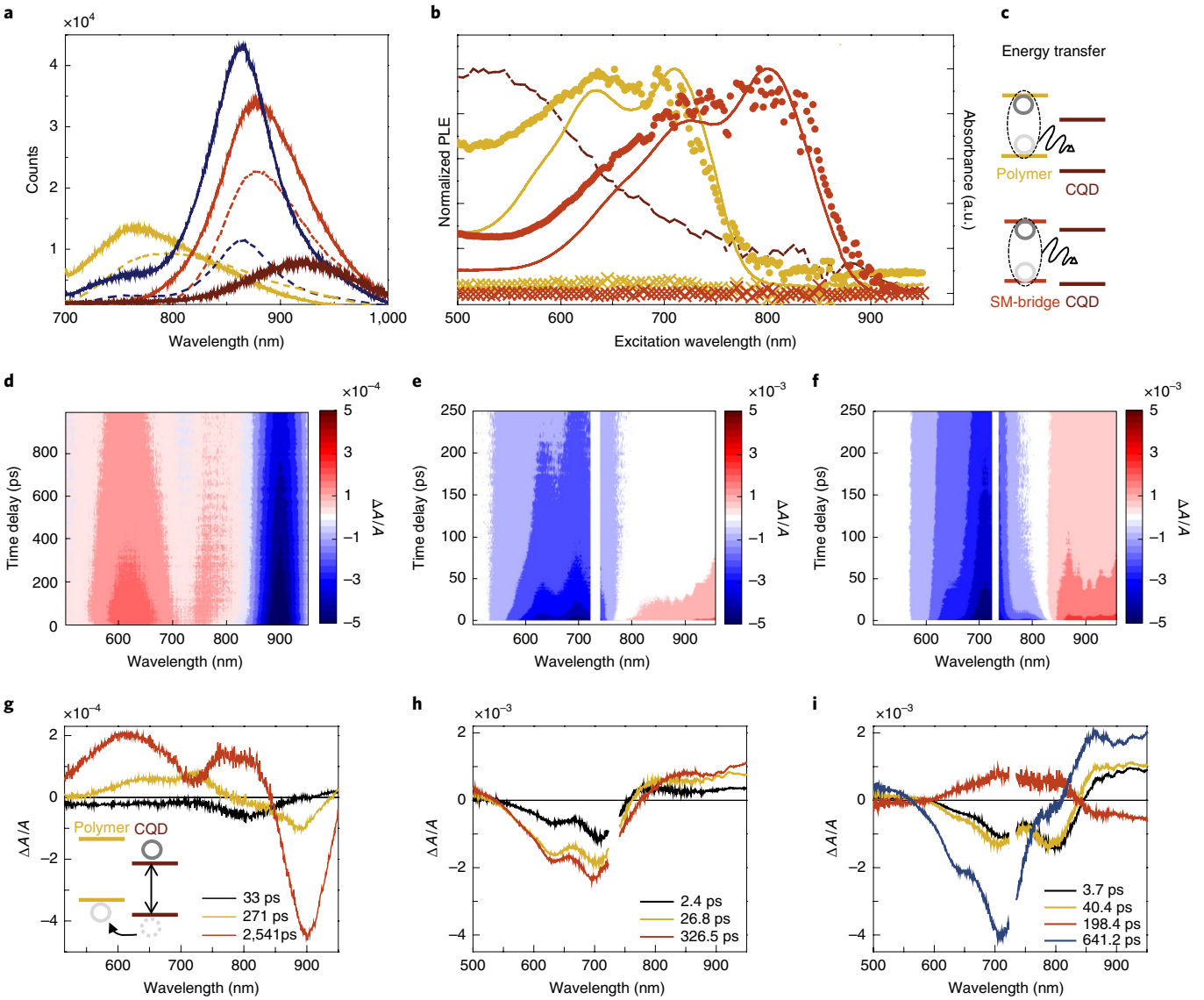

Fig. 2 | Photo-induced carrier dynamics in CQD–organics hybrid films. a, Static PL spectra of polymer (yellow), CQD/polymer (yellow dashes), SM-bridge (red), CQD/SM-bridge (red dashes), polymer–SM-bridge (blue), CQD/polymer–SM-bridge (blue dashes) and CQD (brown) films under 633 nm excitation. **b**, PLE spectroscopy experiments. The detection wavelength is fixed at 1,200 nm (corresponding to emission only from CQDs). The PLE spectra are of the polymer (yellow crosses), the SM-bridge (red crosses), polymer/CQD (yellow circles) and SM-bridge/CQD (red circles) bilayer films. Normalized absorbance spectra of CQDs (brown dashed line), polymer (yellow line) and SM-bridge (red line) layers are plotted. **c**, Schematics depicting energy transfer from organics to CQDs. Dark and light grey circles denote the electron and hole, respectively. **d**,**g**, Spectro-temporal TA maps (**d**) and DAS (**g**) for the CQD/polymer–SM-bridge with direct photoexcitation of the CQDs with near-infrared (930 nm) pump pulses. The inset illustrates hole transfer from the CQD to the polymer. Low excitation fluences were used to minimize Auger recombination in the photoexcited CQD layer[42,44]. **e**,**f**,**h**,**i**, Spectro-temporal TA maps (**e**,**f**) with a photoexcitation wavelength of 730 nm and their DAS (**h**,**i**) for films of polymer/CQD without (**e**,**h**) and with (**f**,**i**) SM-bridge. *A*, absorption.

of flight–secondary ion mass spectroscopy (ToF–SIMs) agrees with the imaged structure (Supplementary Fig. 16).

Next, we characterized the solar cells under simulated solar irradiation and found that the resulting device performance depends heavily on the use of the SM-bridge (Supplementary Fig. 17). Notably, short-circuit current (J_{sc}) was significantly enhanced, from 13 to 23 mA cm^{-2}, on incorporation of the SM-bridge. To investigate the origins of the observed J_{sc} enhancement, we studied the spectral response of our CQD/polymer hybrid devices (Fig. 3b–d). The EQE of the CQD/polymer without the SM-bridge lies below 40% for wavelengths longer than 600 nm. Incorporation of the SM-bridge led to a twofold enhancement in EQE in this wavelength region, in which the organics contribute significantly to the photocurrent.

To gain additional insight into the origins of the observed enhancement in EQE, we measured the total absorption and IQE spectra. CQD/polymer films without the SM-bridge showed a similarly high absorption up to 700 nm, corresponding to the absorption peak of the polymer (Fig. 3d). Near-infrared absorption increases significantly near 800 nm in samples including the SM-bridge, consistent with the absorption peak of the SM-bridge (Fig. 1d).

To determine the contribution of each material to the total absorption, we calculated the net absorption of both CQDs and organic layers using the transfer matrix formalism (Fig. 3e,f). CQD/polymer devices without the SM-bridge exhibit broadband CQD absorption from 300 to 1,000 nm and strong polymer absorption between 550 nm and 750 nm. Samples including the SM-bridge

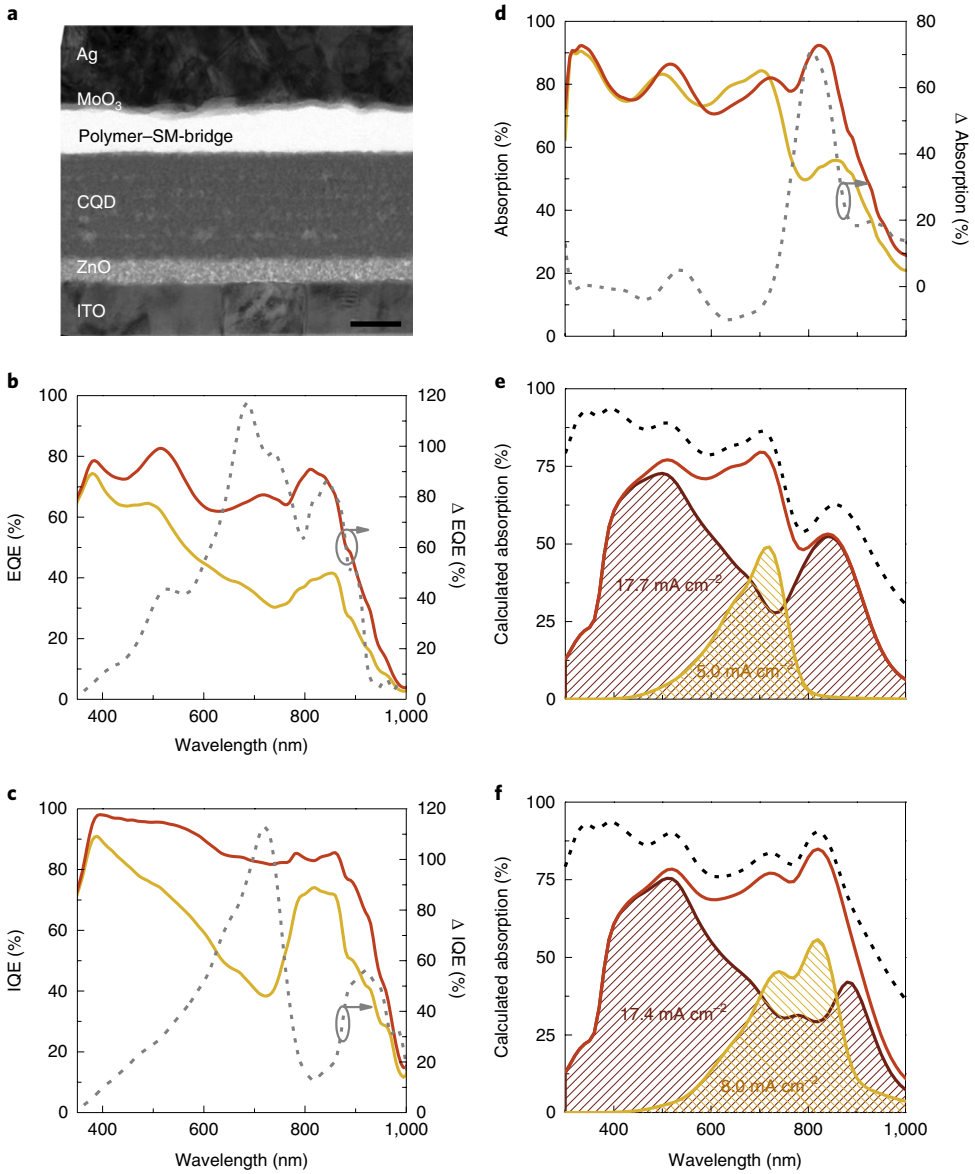

Fig. 3 | Structure and spectral response of hybrid solar cells. a, TEM cross-section of overall device structure. Scale bar, 50 nm. **b**, EQE spectra of CQD/polymer device without (yellow) and with (red) SM-bridge. **c**,**d**, IQE curves (**c**) and experimentally measured absorption spectra (**d**) of CQD/polymer devices without (yellow) and with (red) SM-bridge. Grey dashed lines in **b**–**d** depict relative EQE (**b**), IQE (**c**) or absorption (**d**) enhancement of the CQD/SM-bridge–polymer devices with respect to CQD/polymer devices. **e**, Calculated absorption spectra of CQD (brown), polymer (yellow) and CQD+polymer (red). **f**, Calculated absorption spectra of CQD (brown), polymer+SM-bridge (yellow) and CQD+organics (red). The black dashed lines in **e**,**f** denote the calculated total absorption of the entire device. Brown and yellow dashed areas in **e**,**f** describe the amount of photon collection of CQD and organics, respectively.

show improved total absorption from 750 to 900 nm due to the contribution of the SM-bridge. From these results, we estimated the current density corresponding to the calculated absorption at perfect charge-extraction conditions (that is, IQE = 100%) and observed a 1.6-fold increase in J_{sc} from the polymer (from 5 to 8 mA cm^{-2}) on insertion of the SM-bridge.

We then calculated the IQE spectrum of CQD/polymer hybrids with and without the SM-bridge (Fig. 3c). The CQD/polymer hybrids show a wavelength-dependent IQE particularly in the 600 to 750 nm range, corresponding to the absorption band of the polymer. CQD/SM-bridge–polymer samples, on the other hand, show a consistently higher IQE throughout the entire wavelength range 300–1,000 nm, with an average IQE of 90% as mentioned above. In particular, the IQE dip between 600 and 750 nm disappears, which we ascribe to improved energy transfer and charge-extraction dynamics at organic boundaries, as attested to by spectroscopic investigations.

Performance of CQD/organic hybrid photovoltaics

We optimized the CQD/SM-bridge–polymer hybrid composition to maximize light harvesting efficiency and photovoltaic performance. The CQD layers were prepared by using a solution-phase ligand exchange, resulting in improved performance compared to typical solid-state layer-by-layer exchange processes[34]. We achieved a PCE of 13.1% for CQD/SM-bridge–polymer hybrids, which is significantly higher than for the organic-only (polymer–SM-bridge BHJ) (8.0%) and CQD-only (CQD/EDT-treated CQD) (10.4%) reference devices (Fig. 4a). This represents a most efficient organic/CQD

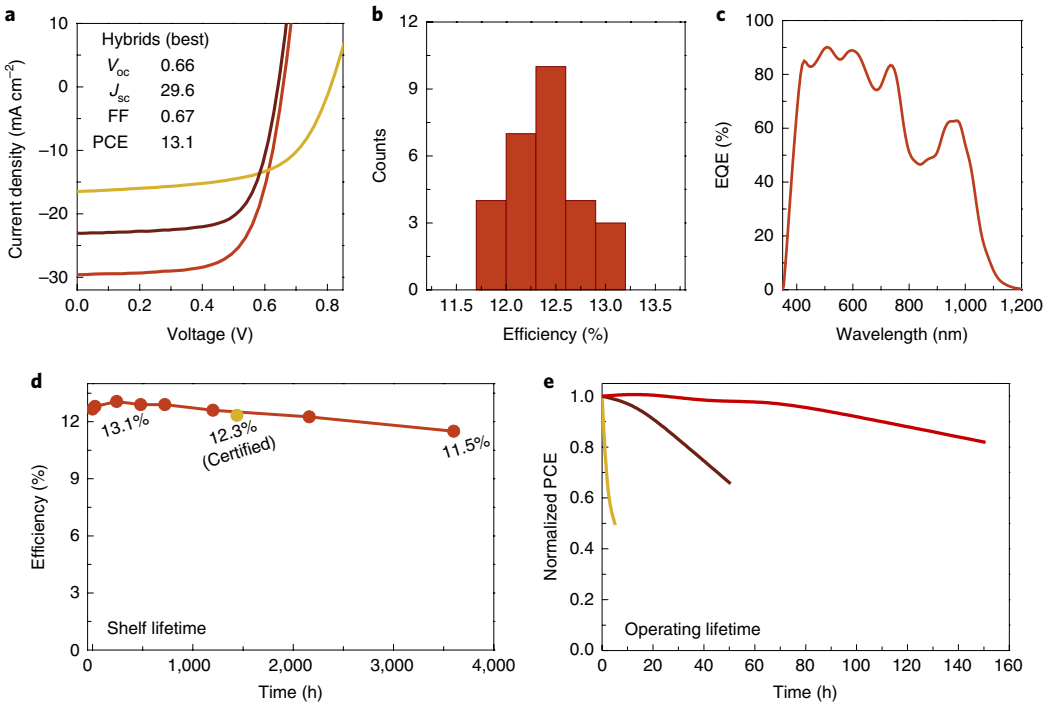

Fig. 4 | Photovoltaic performance. a, Representative *J*–*V* curves of polymer–SM-bridge BHJ (yellow), CQD with EDT layer (brown) and CQD/polymer–SM-bridge (red). FF, fill factor. **b**, Statistical histogram of CQD/polymer–SM-bridge device. **c**, EQE spectra of CQD/polymer–SM-bridge device. **d**, Shelf lifetime of CQD/polymer–SM-bridge device. The devices were stored in ambient conditions without encapsulation. **e**, Operating lifetime of polymer–SM-bridge (yellow), CQD with EDT (brown) and CQD/polymer–SM-bridge (red). All devices were stored in ambient conditions without encapsulation or a filter and ambient relative humidity was ~30–50%. The initial PCEs of the polymer–SM-bridge, CQD with EDT and CQD/polymer–SM-bridge devices were 7.9%, 10.5% and 12.7% respectively.

hybrid structure (Supplementary Fig. 19 and Supplementary Table 3). The PCE histogram of hybrid devices displays an average efficiency of 12.4% (Fig. 4b). Optimized devices exhibit a J_{sc} of 30 mA cm^{-2} for this CQD bandgap, highlighting the benefits of using CQDs and organics together to improve light harvesting. The EQE exceeds 80% in the visible range and reaches 60% in the near infrared (Fig. 4c). In addition, the hybrid structure also showed a higher V_{oc} (0.66 V) compared to the CQD-only (0.64 V) and CQD/polymer without SM-bridge (0.60 V) devices (Supplementary Table 1), attributable to improved charge separation and hole extraction, which in turn suppress recombination—consistent with our observations from TAS (Fig. 2), IQE (Fig. 3) and impedance spectroscopy (Supplementary Fig. 20 and Supplementary Note 6)[35]. The hybrid devices also exhibit good stability, with a certified PCE of 12.3% after 1,500 h of shelf storage under ambient conditions without encapsulation (Supplementary Fig. 21), retaining over 90% of their initial PCE even after 3,500 h (Fig. 4d).

Encouraged by the enhanced shelf stability of the proposed hybrid platform, we then sought to evaluate their stability in more demanding conditions. We tracked the performance under continuous illumination at the MPP, with neither encapsulation, UV filter nor controlled atmosphere (Fig. 4e). The operating lifetime of hybrid devices outperformed organic- and CQD-only devices by a factor of 100 and 5, respectively, retaining over 80% of the initial performance after 150 h. Photo-oxidation of organic molecules due to high-energy UV photons is well known to hinder the stable operation of organic solar cells[36]. In this hybrid architecture, high-energy photons are absorbed in the CQD film before reaching the organic materials, thereby significantly reducing this photodegradation mechanism. The hybrid structures also showed higher stability than CQD-only devices because of efficient oxygen and moisture blocking by the organic layers covering the CQD layer[37]. In addition, the SM-bridge organic layer has a superior stability compared to previous PCBM–CQD hybrids, which exhibited limited photostability due to the oxidation and dimerization of PCBM under irradiation[38,39]. The resulting MPP stability ($t_{80} \approx 150$ h, PCE of 13.1%) of the hybrid structure is high when compared to the organic ($t_{80} \approx 90$ h, PCE of 7.7%) and CQD-based solar cells reported to date[36,40]. The hybrid structure presented herein circumvents the need to rely on filters and highly controlled atmospheres, making it a competitive photovoltaic platform for commercially viable solar energy harvesting.

Conclusions

In this work, we demonstrate a CQD/polymer hybrid platform that outperforms CQD and organic PV devices in both PCE and stability. We achieved this by introducing a SM-bridge in the polymer layer that improves near-infrared absorption and charge separation. This combination leads to a maximum PCE of 13.1% and a certified value of 12.3% following 1,500 h of unencapsulated storage, outperforming previously reported CQD and organic (and hybrid) PV cells. In addition, hybrid devices exhibited excellent stability even under demanding operating conditions. We demonstrated that hybrid devices retain more than 80% of their initial performance after 150 h of continuous operation at MPP under 1-Sun illumination in air, with neither UV filter nor encapsulation. This joint advance in PCE and stability highlights the potential of this hybrid technology to realize inexpensive, air-processed, efficient and stable solution-processed photovoltaics.

Methods

CQD–organics hybrid device fabrication. Oleic acid-capped lead sulfide (PbS) CQDs (first excitonic peak at 850–930 nm) were prepared as previously described[34]. For the fabrication of hybrid devices, a ZnO sol-gel solution, a mixture of zinc

acetate dihydrate:ethanolamine = 1:0.28 wt% dissolved in 10 ml of methoxyethanol, was spin-cast onto a precleaned indium tin oxide (ITO) substrate and dried at 200 °C for 10 min, forming a 30-nm-thick layer. Five layers of the EMII-treated PbS CQDs were coated using a layer-by-layer (LBL) process (Figs. 1–3)[41]. For the hybrid CQDs layer (Fig. 4), we used solution-processed ligand-exchange processes instead of a LBL process as previously reported[34]. Briefly, oleic-capped PbS CQDs were exchanged by the PbX_2/AA solution-phase ligand-exchange process (PbI_2, 0.1 M; $PbBr_2$, 0.02 M; AA (NH_4Ac), 0.04 M). Exchanged dots were precipitated and dried in a vacuum chamber for 10 min. The final CQDs were dispersed in butylamine, forming a CQD ink at a concentration of 250 mg ml^{-1} and spin-coated at 2,500 r.p.m. for 30 s. After 1 d of air drying, a prepared solution of PBDTTT-E-T:IEICO (1:1 wt%, with 15 mg ml^{-1} in chlorobenzene: 1,8-diiodoctane = 98:2 wt%) was spin-coated at 3,000 r.p.m. for 60 s. Organic molecules were purchased from 1-materials. All films were coated onto the substrate under ambient conditions. Subsequently, the film was dried at 100 °C for 5 min. Finally, the MoO_3 (10 nm)/Ag (150 nm) electrode was deposited using thermal evaporation under high vacuum (<10^{-6} torr) through a shadow mask.

CQD/polymer bilayer solar cells. For the fabrication of CQD/polymer devices, a ZnO sol-gel solution was spin-cast onto pre-cleaned ITO substrates and dried at 200 °C for 10 min. Five layers of the EMII-treated PbS CQDs were coated using a LBL process. After 1 d of air drying, the various polymer solutions (10 mg ml^{-1} in chlorobenzene) were spin-coated at 3,000 r.p.m. for 30 s. Subsequently, the films were dried at 100 °C for 5 min. Finally, MoO_3 (10 nm)/Ag (150 nm) electrodes were deposited using thermal evaporation. All films were coated on the substrate under ambient conditions.

CQD/polymer BHJ solar cells. For the fabrication of CQD/polymer BHJ devices, a ZnO sol-gel solution was spin-cast onto precleaned ITO substrates. Oleic acid-capped PbS CQDs were mixed with polymer solutions (5 mg ml^{-1} in chloroform) and spin-coated at 3,000 r.p.m. for 30 s under ambient conditions. The resultant films were treated using the EMII ligand and dried in ambient conditions. Finally, the MoO_3 (10 nm)/Ag (150 nm) electrodes were deposited using thermal evaporation.

TA measurement. Femtosecond laser pulses (1,030 nm, 5 kHz repetition rate) were produced using a regeneratively amplified Yb:KGW (potassium gadolinium tungstate) laser (PHAROS, Light Conversion). The majority part of the fundamental beam was used to pump an optical parametric amplifier (ORPHEUS, Light Conversion) while the minority part was focused into a sapphire crystal to generate a white-light continuum probe. The pump pulse duration was estimated to be ~200 fs. Both the pump and probe pulses were directed into a commercial TA spectrometer (Helios, Ultrafast). Delaying the probe pulse relative to the pump provides a time window of up to 8 ns. Measurements were performed using an average power of less than 50 µW with a spot size of ~0.40 µm^2 at wavelengths of 730 or 930 nm. These fluences are sufficiently low to avoid Auger recombination in the directly photoexcited CQDs or exciton–exciton annihilation in the organics[42].

PL and PLE measurements. PL characterization was performed using a Horiba Fluorolog system. Static PL was collected by illuminating the samples using a monochromatic Xe lamp. The excitation wavelength was 633 nm and emission was scanned from 700 nm to 1,200 nm. For PLE measurements, PL signals were detected at 1,200 nm to probe only CQD PL. Excitation wavelengths were scanned from 500 nm to 950 nm in 5 nm steps. The PL signal of the organics was negligible beyond 1,100 nm (Supplementary Fig. 23), implying that the PLE signal solely originated from CQDs. Larger-sized (smaller-bandgap) CQD (excitonic peak ~1,050 nm) films were used for PLE measurements to obtain a clear, non-overlapping PL feature near 1,200 nm (Supplementary Fig. 23). All films were prepared on the glass substrates using the same method as in the device fabrication.

Time-resolved photoluminescence (TRPL) measurement. For the TRPL measurements, a Hamamatsu C9300 streak camera system with a time resolution of 15 ps was employed. The excitation source for the TRPL was a Libra 1 kHz femtosecond Ti:sapphire regenerative amplifier system with a central wavelength of 780 nm and an 80 fs pulse duration. About 95% of the laser beam was sent to a Coherent TOPAS Prime optical parametric amplifier to be used as a tunable beam. TRPL traces were measured in the wavelength region of 750–850 nm under 700 nm excitation.

Solar cell characterizations. The *J*–*V* curves of the photovoltaic devices were characterized using a Keithley 2400 sourcemeter under 1-Sun illumination with AM 1.5G solar spectrum (Sciencetech, class AAA) from an Xe lamp (Solar Light Company Inc.). The irradiance was calibrated using a reference Si solar cell (Newport, Inc.) to 100 mW cm^{-2} and the aperture size of each device was 0.0625 cm^2. The EQE was measured using a spectral measurement system (K3100 IQX, McScience Inc.). The spectral reflection of the solar cells was measured immediately after the EQE measurement at the same position.

Stability tests. Shelf lifetime was obtained from devices stored in air without encapsulation. For the operating lifetime at MPP, the device was held at the voltage at the maximum power point (V_{mpp}). The unencapsulated device was under 1-Sun illumination. All devices were characterized under ambient conditions and the humidity and temperature were typically in the range of 30–50% and 27–30 °C, respectively. Stability was characterized for devices with the highest PCE in the various configurations depicted in Fig. 4a.

Optical calculations. For the calculations, all refractive indices were obtained by variable angle spectroscopic ellipsometric and a home-made MATLAB code was used to implement the transfer matrix formalism[43] (Supplementary Fig. 18). Thicknesses were obtained from TEM images. We assumed that each layer was flat and considered no scattering effects. Note that the current density as described in Fig. 3d corresponds to the assumption of a perfect maximum value of the carrier extraction (that is, IQE = 100%).

Absorbance measurements. Absorbance spectra were measured using a UV–visible–infrared spectrophotometer (Lambda 950).

SEM, TEM and TOF–SIMs. The cross-section electron microscope image of the hybrid device was obtained by focused-ion-beam (Helios 450 F1) and field-emission TEM (300 keV). TOF–SIMs (TOF–SIMS5, ION-TOF GmbH) was measured to clarify the device structure.

AFM measurements. AFM imaging (BRUKER, multimode 8) was performed in scanasyst mode with 1 Hz scanning speed.

Ultraviolet photoelectron spectroscopy. Ultraviolet photoelectron spectroscopy (Sigma Probe, Thermo VG Scientific) was performed to characterize the energy level of each material.

Reporting Summary. Further information on research design is available in the Nature Research Reporting Summary linked to this article.

Data availability

The authors declare that the main data supporting the findings of this study are available within the article and its Supplementary Information. Extra data are available from the authors upon request.

Received: 19 September 2018; Accepted: 3 October 2019;
Published online: 11 November 2019

References

1. Tan, H. et al. Efficient and stable solution-processed planar perovskite solar cells via contact passivation. *Science* **355**, 722–726 (2017).
2. Hou, J. H., Inganas, O., Friend, R. H. & Gao, F. Organic solar cells based on non-fullerene acceptors. *Nat. Mater.* **17**, 119–128 (2018).
3. Yuan, M. J., Liu, M. X. & Sargent, E. H. Colloidal quantum dot solids for solution-processed solar cells. *Nat. Energy* **1**, 16016 (2016).
4. Kagan, C. R., Lifshitz, E., Sargent, E. H. & Talapin, D. V. Building devices from colloidal quantum dots. *Science* **353**, 5523 (2016).
5. Xu, J. et al. 2D matrix engineering for homogeneous quantum dot coupling in photovoltaic solids. *Nat. Nanotechnol.* **13**, 456–462 (2018).
6. Chuang, C. H. M., Brown, P. R., Bulovic, V. & Bawendi, M. G. Improved performance and stability in quantum dot solar cells through band alignment engineering. *Nat. Mater.* **13**, 796–801 (2014).
7. Huynh, W. U., Dittmer, J. J. & Alivisatos, A. P. Hybrid nanorod-polymer solar cells. *Science* **295**, 2425–2427 (2002).
8. Muller-Buschbaum, P., Thelakkat, M., Fassler, T. F. & Stutzmann, M. Hybrid photovoltaics—from fundamentals towards application. *Adv. Energy Mater.* **7**, 248 (2017).
9. Piliego, C. et al. Charge separation dynamics in a narrow band gap polymer–PbS nanocrystal blend for efficient hybrid solar cells. *J. Mater. Chem.* **22**, 24411–24416 (2012).
10. Seo, J., Cho, M. J., Lee, D., Cartwright, A. N. & Prasad, P. N. Efficient heterojunction photovoltaic cell utilizing nanocomposites of lead sulfide nanocrystals and a low-bandgap polymer. *Adv. Mater.* **23**, 3984–3988 (2011).
11. Seo, J. et al. Enhancement of the photovoltaic performance in PbS nanocrystal: P3HT hybrid composite devices by post-treatment-driven ligand exchange. *Nanotechnology* **20**, 095202 (2009).
12. Speirs, M. J. et al. Hybrid inorganic–organic tandem solar cells for broad absorption of the solar spectrum. *Phys. Chem. Chem. Phys.* **16**, 7672–7676 (2014).
13. Noone, K. M. et al. Broadband absorbing bulk heterojunction photovoltaics using low-bandgap solution-processed quantum dots. *Nano. Lett.* **10**, 2635–2639 (2010).
14. Lu, H., Joy, J., Gaspar, R. L., Bradforth, S. E. & Brutchey, R. L. Iodide-passivated colloidal PbS nanocrystals leading to highly efficient polymer: nanocrystal hybrid solar cells. *Chem. Mater.* **28**, 1897–1906 (2016).

15. Liao, S. H., Jhuo, H. J., Cheng, Y. S. & Chen, S. A. Fullerene derivative-doped zinc oxide nanofilm as the cathode of inverted polymer solar cells with low-bandgap polymer (PTB7-Th) for high performance. *Adv. Mater.* **25**, 4766–4771 (2013).
16. Liang, Y. Y. et al. For the bright future-bulk heterojunction polymer solar cells with power conversion efficiency of 7.4%. *Adv. Mater.* **22**, 135–138 (2010).
17. You, J. B. et al. A polymer tandem solar cell with 10.6% power conversion efficiency. *Nat. Commun.* **4**, 1446 (2013).
18. Martinez, L., Bernechea, M., de Arquer, F. P. G. & Konstantatos, G. Near IR-sensitive, non-toxic, polymer/nanocrystal solar cells employing Bi2S3 as the electron acceptor. *Adv. Energy Mater.* **1**, 1029–1035 (2011).
19. Liu, Z. K. et al. High-efficiency hybrid solar cells based on polymer/PbS_xSe_{1-x} nanocrystals benefiting from vertical phase segregation. *Adv. Mater.* **25**, 5772 (2013).
20. Colbert, A. E., Wu, W., Janke, E. M., Ma, F. & Ginger, D. S. Effects of ligands on charge generation and recombination in hybrid polymer/quantum dot solar cells. *J. Phys. Chem. C.* **119**, 24733–24739 (2015).
21. Couderc, E., Greaney, M. J., Brutchey, R. L. & Bradforth, S. E. Direct spectroscopic evidence of ultrafast electron transfer from a low band gap polymer to CdSe quantum dots in hybrid photovoltaic thin films. *J. Am. Chem. Soc.* **135**, 18418–18426 (2013).
22. Jarzab, D. et al. Charge-separation dynamics in inorganic–organic ternary blends for efficient infrared photodiodes. *Adv. Funct. Mater.* **21**, 1988–1992 (2011).
23. Itskos, G. et al. Optical properties of organic semiconductor blends with near-infrared quantum-dot sensitizers for light harvesting applications. *Adv. Energy Mater.* **1**, 802–812 (2011).
24. Kim, G.-H. et al. Synergistic photocurrent addition in hybrid quantum dot: Bulk heterojunction solar cells. *Nano Energy* **13**, 491–499 (2015).
25. Chen, H. Y. et al. A p-type quantum dot/organic donor: acceptor solar-cell structure for extended spectral response. *Adv. Energy Mater.* **1**, 528–533 (2011).
26. Yao, H. F. et al. Design and synthesis of a low bandgap small molecule acceptor for efficient polymer solar cells. *Adv. Mater.* **28**, 8283–8287 (2016).
27. Cnops, K. et al. 8.4% efficient fullerene-free organic solar cells exploiting long-range exciton energy transfer. *Nat. Commun.* **5**, 3406 (2014).
28. Huang, J.-S. et al. Polymer bulk heterojunction solar cells employing Förster resonance energy transfer. *Nat. Photonics* **7**, 479 (2013).
29. Gupta, V., Bharti, V., Kumar, M., Chand, S. & Heeger, A. J. Polymer–polymer förster resonance energy transfer significantly boosts the power conversion efficiency of bulk-heterojunction solar cells. *Adv. Mater.* **27**, 4398–4404 (2015).
30. Penwell, S. B., Ginsberg, L. D. S., Noriega, R. & Ginsberg, N. S. Resolving ultrafast exciton migration in organic solids at the nanoscale. *Nat. Mater.* **16**, 1136–1141 (2017).
31. Knutson, J. R., Beechem, J. M. & Brand, L. Simultaneous analysis of multiple fluorescence decay curves: a global approach. *Chem. Phys. Lett.* **102**, 501–507 (1983).
32. Jakowetz, A. C. et al. What controls the rate of ultrafast charge transfer and charge separation efficiency in organic photovoltaic blends. *J. Am. Chem. Soc.* **138**, 11672–11679 (2016).
33. Cui, Y. et al. Fine-tuned photoactive and interconnection layers for achieving over 13% efficiency in a fullerene-free tandem organic solar cell. *J. Am. Chem. Soc.* **139**, 7302–7309 (2017).
34. Liu, M. et al. Hybrid organic–inorganic inks flatten the energy landscape in colloidal quantum dot solids. *Nat. Mater.* **16**, 258–263 (2017).
35. Fabregat-Santiago, F., Garcia-Belmonte, G., Mora-Seró, I. & Bisquert, J. Characterization of nanostructured hybrid and organic solar cells by impedance spectroscopy. *Phys. Chem. Chem. Phys.* **13**, 9083–9118 (2011).
36. Baran, D. et al. Reducing the efficiency–stability–cost gap of organic photovoltaics with highly efficient and stable small molecule acceptor ternary solar cells. *Nat. Mater.* **16**, 363–369 (2017).
37. Baek, S.-W. et al. A hydro/oxo-phobic top hole-selective layer for efficient and stable colloidal quantum dot solar cells. *Energy Environ. Sci.* **11**, 2078–2084 (2018).
38. Distler, A. et al. The effect of PCBM dimerization on the performance of bulk heterojunction solar cells. *Adv. Energy Mater.* **4**, 1300693 (2014).
39. Holliday, S. et al. High-efficiency and air-stable P3HT-based polymer solar cells with a new non-fullerene acceptor. *Nat. Commun.* **7**, 11585 (2016).
40. Zhang, X. et al. Inorganic $CsPbI_3$ perovskite coating on PbS quantum dot for highly efficient and stable infrared light converting solar cells. *Adv. Energy Mater.* **8**, 1702049 (2018).
41. Cao, Y. M., Stavrinadis, A., Lasanta, T., So, D. & Konstantatos, G. The role of surface passivation for efficient and photostable PbS quantum dot solar cells. *Nat. Energy* **1**, 16035 (2016).
42. Proppe, A. H. et al. Picosecond charge transfer and long carrier diffusion lengths in colloidal quantum dot solids. *Nano Lett.* **18**, 7052–7059 (2018).
43. Pettersson, L. A., Roman, L. S. & Inganäs, O. Modeling photocurrent action spectra of photovoltaic devices based on organic thin films. *J. Appl. Phys.* **86**, 487–496 (1999).
44. Sandeep, C. S. S. et al. High charge-carrier mobility enables exploitation of carrier multiplication in quantum-dot films. *Nat. Commun.* **4**, 2360 (2013).

Acknowledgements

This research was supported by Ontario Research Fund–Research Excellence program (ORF7–Ministry of Research and Innovation, Ontario Research Fund–Research Excellence Round 7); and by the Natural Sciences and Engineering Research Council (NSERC) of Canada. This work was supported by National Research Foundation of Korea (NRF) grants (nos. NRF-2015M1A2A2057509 and NRF-2019R1A2C3008035). J.H.S. and S. Jeong were supported by grant no. NRF-2019M3D1A1078296. A.H.P. was supported by an NSERC CGS-D fellowship.

Author contributions

S.-W.B., F.P.G.A., S.O.K., S.H. and O.V. developed the idea and prepared the manuscript. S. Jun, G.W., A.H.P., H.R.B. and M.S.J. studied and characterized the carrier dynamics. C.K. and B.K. optimized the record device structure. J.K., J.H.S. and S. Jeong synthesized the CQDs dots and characterized the films. O.O. performed the optical calculations. J.-Y. L. and E.H.S. supervised the project. All authors discussed the results and commented on the manuscript.

Competing interests

The authors declare no competing interests.

Additional information

Supplementary information is available for this paper at https://doi.org/10.1038/s41560-019-0492-1.

Correspondence and requests for materials should be addressed to J.-Y.L. or E.H.S.

Reprints and permissions information is available at www.nature.com/reprints.

Publisher's note Springer Nature remains neutral with regard to jurisdictional claims in published maps and institutional affiliations.

nature research

Corresponding author(s): Edward H. Sargent

Solar Cells Reporting Summary

Nature Research wishes to improve the reproducibility of the work that we publish. This form is intended for publication with all accepted papers reporting the characterization of photovoltaic devices and provides structure for consistency and transparency in reporting. Some list items might not apply to an individual manuscript, but all fields must be completed for clarity.

For further information on Nature Research policies, including our data availability policy, see Authors & Referees.

Experimental design

Please check: are the following details reported in the manuscript?

1. Dimensions

Area of the tested solar cells	☒ Yes ☐ No	Described in the Methods (0.0625 cm2)
Method used to determine the device area	☒ Yes ☐ No	Described in the Methods

2. Current-voltage characterization

Current density-voltage (J-V) plots in both forward and backward direction	☒ Yes ☐ No	Described in Supplementary Fig. 21
Voltage scan conditions *For instance: scan direction, speed, dwell times*	☒ Yes ☐ No	Described in Supplementary Fig. 21
Test environment *For instance: characterization temperature, in air or in glove box*	☒ Yes ☐ No	Described in Supplementary Fig. 21 and Methods
Protocol for preconditioning of the device before its characterization	☒ Yes ☐ No	Described in Supplementary Fig. 21 (no precondition)
Stability of the J-V characteristic *Verified with time evolution of the maximum power point or with the photocurrent at maximum power point; see ref. 7 for details.*	☒ Yes ☐ No	Described in Supplementary Fig. 21

3. Hysteresis or any other unusual behaviour

Description of the unusual behaviour observed during the characterization	☒ Yes ☐ No	Described in Supplementary Fig. 21 (no hysterisis)
Related experimental data	☒ Yes ☐ No	Described in Supplementary Fig. 21

4. Efficiency

External quantum efficiency (EQE) or incident photons to current efficiency (IPCE)	☒ Yes ☐ No	Displayed in Fig. 4c.
A comparison between the integrated response under the standard reference spectrum and the response measure under the simulator	☒ Yes ☐ No	Figs. 4a and 4b (less then %5)
For tandem solar cells, the bias illumination and bias voltage used for each subcell	☐ Yes ☒ No	Method (all devices are single-junction solar cells)

5. Calibration

Light source and reference cell or sensor used for the characterization	☒ Yes ☐ No	Described in the Method section
Confirmation that the reference cell was calibrated and certified	☒ Yes ☐ No	Described in the Method section

Calculation of spectral mismatch between the reference cell and the devices under test	☒ Yes ☐ No	Described in the Method section

6. Mask/aperture

Size of the mask/aperture used during testing	☒ Yes ☐ No	Described in the Method section
Variation of the measured short-circuit current density with the mask/aperture area	☐ Yes ☒ No	We always tested device performance at the same mask/aperture area.

7. Performance certification

Identity of the independent certification laboratory that confirmed the photovoltaic performance	☒ Yes ☐ No	Certificated by Newport
A copy of any certificate(s) *Provide in Supplementary Information*	☒ Yes ☐ No	Displayed in Supplementary Fig. 21

8. Statistics

Number of solar cells tested	☒ Yes ☐ No	Described in Fig. 4b
Statistical analysis of the device performance	☒ Yes ☐ No	Described in Fig. 4b

9. Long-term stability analysis

Type of analysis, bias conditions and environmental conditions *For instance: illumination type, temperature, atmosphere humidity, encapsulation method, preconditioning temperature*	☒ Yes ☐ No	Depicted in Figures 4d, 4e and the Method section